$Mg_xMn_{2-x}B_2O_5$ Pyroborates ($\frac{2}{3} \leq x \leq \frac{4}{3}$): High Capacity and High Rate Cathodes for Li-ion batteries

Hugh F. J. Glass[1,2], Zigeng Liu[2], Paul M. Bayley[2], Emmanuelle Suard[3], Shou-Hang Bo[4,5], Peter G. Khalifah[4,6], Clare P. Grey[2] and Siân E. Dutton[1]*

[1] Cavendish Laboratory, Department of Physics, University of Cambridge, JJ Thomson Avenue, Cambridge CB3 0HE, U.K.

[2] Department of Chemistry, University of Cambridge, Lensfield Road, Cambridge CB2 1EW, U.K.

[3] Institut Laue-Langevin, 71 avenue des Martyrs, 38000 Grenoble, France

[4] Department of Chemistry, State University of New York at Stony Brook, New York, 11794-3400, United States

[5] Materials Science Division, Lawrence Berkeley National Laboratory, Berkeley, California 94720, United States

[6] Chemistry Department, Brookhaven National Laboratory, Upton, New York, 11973, United States

$MgMnB_2O_5$, $Mg_{2/3}Mn_{4/3}B_2O_5$ and $Mg_{4/3}Mn_{2/3}B_2O_5$ pyroborates have been prepared via a ceramic method. On charging $MgMnB_2O_5$ vs Li, all of the Mg^{2+} can be removed, and on subsequent cycles 1.4 Li ions, corresponding to a capacity of 250 $mAhg^{-1}$, can be reversibly intercalated. This is achieved at a C/25 rate with 99.6% coulombic efficiency. Significant capacity is retained at high rates with 97 $mAhg^{-1}$ at a rate of 2C. Continuous cycling at moderate rates gradually improves performance leading to insertion of 1.8 Li, 314 $mAhg^{-1}$ with a specific energy of 802 $WhKg^{-1}$, after 1000 cycles at C/5. Ex-situ X-ray and neutron diffraction demonstrate the retention of the pyroborate structure on cycling vs Li and a small volume change (1%) between the fully lithiathed and de-lithiated structures. $Mg_{2/3}Mn_{4/3}B_2O_5$ and $Mg_{4/3}Mn_{2/3}B_2O_5$ are also shown to reversibly intercalate Li at 17.8 $mAhg^{-1}$ and 188.6 $mAhg^{-1}$ respectively, with Mn ions likely blocking Mg/Li transport in the $Mg_{2/3}Mn_{4/3}B_2O_5$ material. The electrochemical ion-exchange of polyanion materials with labile Mg ions could prove to be a route to high energy density Li-ion cathodes.

INTRODUCTION

High capacity, long cycle life and low cost Li-ion batteries (LIBs) have become the most common power source for consumer electronics. However, there is increasing demand for materials that deliver even higher energy densities, with improved safety and at a decreased cost, to aid the commercialization of electric vehicles and grid-scale storage.[1] Currently most commercial cells use transition metal oxides such as $LiCoO_2$ and its Ni-, Mn- and Al- substituted variants (NMC, NCA), or $LiMn_2O_4$ as the cathode,[2–9] but their high cost, toxicity, instability and low energy densities mean there is significant drive to find alternatives.

Polyanion materials such as $LiMPO_4$ and $LiMBO_3$ have attracted interest since they provide high theoretical capacities and tuneable voltages. The benefits of a polyanion framework were first shown for olivine $LiFePO_4$, where the PO_4^{3-} group significantly raises the redox potential compared to oxides and fixed O^{2-} ions providing structural stability.[10] Although the electrical and ionic conductivity are poor, full theoretical capacity (170 $mAhg^{-1}$) has been achieved through forming nano-sized $LiFePO_4$-carbon composites.[11,12] The borate (BO_3^{3-}) framework is the lightest polyanion group and therefore gives the highest theoretical capacities ($LiFePO_4$ = 170 $mAhg^{-1}$, $LiFeBO_3$ = 220 $mAhg^{-1}$). Li$M$$BO_3$ where M = Mn, Co and Fe have been studied and although initial electrochemical performance was poor, subsequent research has steadily improved the reversible capacity to around 75% of theoretical.[13–17] Good cycle life at high voltages, especially for the Mn and Fe borates, means there is continued interest in these systems.

The pyroborate ($M_2B_2O_5$) is another class of borate polyanion that contains a divalent redox active transition metal. The structure of the pyroborates, Figure 1, is versatile with many divalent ions able to occupy the two M sites (e.g. M = Mg, Mn, Fe, Co, Sr, Ca) and both triclinic and monoclinic polymorphs have been synthesised.[18–21] A further advantage of the light weight pyroborate unit is that unlike pyrophosphates, where the heavier $P_2O_7^{4-}$ group compromises the overall capacity[22], the lighter boron atom

(and fewer oxygen atoms) means that a move from borates to pyroborates does not compromise the theoretical capacity. $Mg_xFe_{2-x}B_2O_5$ has been synthesised and proposed as a potential Mg-ion battery cathode material as the Mg ions are mobile,[23] however to our knowledge this family of materials has not been studied in Li-ion batteries.

Here we study the mixed metal phase $Mg_xMn_{2-x}B_2O_5$ (where x = 2/3, 1 or 4/3) for both Mg removal and subsequent cycling vs Li in a LIB. Mn was chosen as the transition metal as in the Li*M*BO3 system, Mn provided moderate rate capability and high capacity, and the ion can, in principle, cycle utilizing two electron couples (between Mn^{2+} and Mn^{4+}). $MgMnB_2O_5$ has been previously synthesised[18] and was found to crystallise in the triclinic phase of $Mg_2B_2O_5$ rather than the monoclinic structure adopted by $Mn_2B_2O_5$. To study the effect of composition on performance, three compounds across the series were prepared, $Mg_{4/3}Mn_{2/3}B_2O_5$, $MgMnB_2O_5$ and $Mg_{2/3}Mn_{4/3}B_2O_5$.

For each phase manganese has an oxidation state of 2+ in the pristine material, and the total theoretical capacity of the three materials is then a function of both the total Mn content and the available Mg for extraction as we now illustrate: for x = 4/3 ($Mg_{4/3}Mn_{2/3}B_2O_5$) the capacity obtained on oxidising all the Mn^{2+} to Mn^{4+} forming $Mg_{2/3}Mn_{2/3}B_2O_5$ corresponds to 207.9 $mAhg^{-1}$. Since the mass of the lithiated sample is lower, a slightly higher theoretical capacity is obtained on full lithiation (231 $mAhg^{-1}$), where we have assumed reduction back to Mn^{2+} and the insertion of 2 Li ions per Mg removed to form $Li_{4/3}Mg_{2/3}Mn^{2+}_{2/3}B_2O_5$. For x = 1 the Mg:Mn ratio is optimal and demagnesiation to form $Mn^{4+}B_2O_5$ gives the highest theoretical capacity of 296.6 $mAhg^{-1}$ and 342.5 $mAhg^{-1}$ for lithiation to form $Li_2Mn^{2+}B_2O_5$. For x = 4/3, there is insufficient Mg in the material to oxidise all the Mn^{2+} to Mn^{4+} and a Mn^{3+} compound in theory results in $Mn^{3+}_{4/3}B_2O_5$, with a lower associated capacity of 187 $mAhg^{-1}$, lithiation producing $Li_{4/3}Mn^{2+}_{4/3}B_2O_5$ with a theoretical capacity of 204.1 $mAhg^{-1}$. In the subsequent text all reported cycle rates are based on Mg removal capacities.

In this study we investigate the cation ordering in the three synthesised materials and the change in crystal structure on cycling via X-ray and neutron diffraction. The ability to remove Mg-ions from the structure and the reversibility of Li-ion insertion is assessed.

We find that the Mn and Mg are disordered over the two metal sites with some preference for Mn to occupy the larger, more distorted, site 1, Figure 1. In the material with the highest theoretical capacity, $MgMnB_2O_5$, we show that Mg can be fully removed from the structure, and subsequent cycling vs a Li anode gives up to 250 $mAhg^{-1}$ reversible capacity. The high Mg content $Mg_{4/3}M_{2/3}B_2O_5$ phase intercalates 0.75 Li per formula unit, 188.6 $mAhg^{-1}$ at C/25. However, the Li intercalation behaviour differs for the low Mg content $Mg_{2/3}M_{4/3}B_2O_5$ phase with < 20 $mAhg^{-1}$ reversible capacity and a significant overpotential.

EXPERIMENTAL SECTION

Mixed metal pyroborates were synthesised by grinding stoichiometric amounts of $MnC_2O_4.2H_2O$ (Alfa Aesar 30% Mn min), MgO (Alfa Aesar 99.998%) and H_3BO_3 (Alfa Aesar 99.99%) into a fine powder. The mixture was heated to 400°C at 1°C min^{-1} and held for 10 hours under flowing argon. The powder was reground then heated to 1050°C at 3°C min^{-1} and left at this temperature for 24 hours under flowing argon. The sample was then furnace cooled. ^{11}B enriched samples prepared for neutron powder diffraction were synthesised from ^{11}B-Boric acid (Aldrich 99%).

Powder diffraction experiments (PXRD) were carried out on a PANalytical Empyrean Series 2 Diffractometer System with CuKα radiation (λ = 1.540598 Å, 1.544340 Å). Rietveld analysis[24] was performed using the FullProf suite of programs[25] over a 2θ range of 10°-70°, with step size of 2θ =0.0167°. Backgrounds were fitted using a linear interpolation of data points. The peak shape was modelled using a pseudo-Voigt function and peak broadening was modelled using a symmetry dependent Scherrer analysis.[26] This analysis uses a spherical harmonic expansion dependant on the Laue class of the crystal. Micro-particle size is then inferred by comparison with the peak widths of a crystalline silicon standard.

PXRD was carried out on ex-situ samples by packing the cycled material into a 0.3 mm capillary and sealing with capillary wax. Quantitative analysis to determine the symmetry and lattice parameters was carried by profileless pattern fitting,[27] in the Fullprof suite of programs. [25]

Constant wavelength neutron diffraction data were collected over a 2θ range of 10°-160°, with step size of 2θ = 0.050018° on D2B instrument (λ = 1.596 Å) at Institut Laue-Langevin (ILL, Grenoble). Pristine and cycled samples were packed under inert conditions in sealed vanadium canisters and measured for 12 hours. As ^{10}B has a large absorbance cross section ^{11}B enriched samples were measured, and a corresponding neutron scattering length were used during analysis. Rietveld analysis[24] was performed using the FullProf suite of programs[25]. Backgrounds were fitted using a linear interpolation of data points. The peak shape was modelled using a pseudo-Voigt function. For cycled samples profileless pattern matching[27] was used in FullProf to calculate cell volume.

^7Li NMR spectra of the cycled materials were acquired in a 1.3 mm probe head on a Bruker 500 MHz and 200 MHz spectrometer, with Magic angle spinning (MAS) up to 50 kHz. Li_2CO_3 was used as a 0 ppm reference. Data was analysed using Bruker TopSpin 3.5.

Magnetic measurements were carried out using a Quantum Design magnetic properties measurement system (MPMS3) superconducting quantum interference device (SQUID) magnetometer. The magnetization (M) was measured in a field of 1000 Oe as a function of temperature on warming from 2 to 300 K after cooling in zero field (ZFC). Magnetic susceptibility, $\chi = \frac{\partial M}{\partial H}$, was assumed to be linear in the small measuring field, therefore $\chi = \frac{M}{H}$. Effective moments were calculated using a linear fit to the Curie-Weiss law, $\chi = \frac{C}{T-\theta}$ where the curie constant, $C = \frac{N\mu}{K_\beta}\mu_{eff}^2 \approx 8\mu_{eff}^2$, from 150-300 K.

As carbon and PTFE make up a significant portion of the cathode material there is a diamagnetic contribution to the

measured magnetisation of ex-situ samples. This was accounted for by comparing the magnetisation of the pristine material with the uncycled cathode material and calculating a diamagnetic contribution per gram of carbon/PTFE, which was then applied to the ex-situ samples.

Electrochemical properties were investigated using an Arbin BT2000 potentiostat. Stainless steel CR2032 cells were constructed with a Li metal anode, cathode film and glass fibre separator soaked in LP30 electrolyte (1M $LiPF_6$ in 50/50 v/v ethylene carbonate and dimethyl carbonate, EC/DMC). Cathode films were prepared by ball milling $Mg_xMn_{2-x}B_2O_5$ under argon for 4×5 minutes, then mixed with 33 wt% Ketjen Black and ball milled for a further 10 minutes. The resultant powder had an average particle size of 60nm and was mixed with 10 wt% PTFE to form the cathode film.

All ex-situ samples were disassembled within one hour of cycle completion and washed with dimethyl carbonate to remove electrolyte.

RESULTS AND DISCUSSION

Structure

PXRD and powder neutron diffraction analysis of $Mg_xMn_{2-x}B_2O_5$ (x = 2/3, 1, 4/3) indicated formation of phase pure products. Rietveld refinement showed that all three materials adopt the triclinic phase rather than the monoclinic structure found for $Mn_2B_2O_5$[18,21]. In the triclinic pyroborate structure, shown in Figure 1, the $B_2O_5^{4-}$ unit is formed from two corner-sharing BO_3 triangles. The $B_2O_5^{4-}$ groups link ribbons of edge-sharing MO_6 octahedra. Within the ribbons there are two crystallographically distinct sites, *M*1 and *M*2. The *M1* site (blue octahedra Figure 1a) is more distorted than *M*2 (purple octahedra) with larger bond angle variance.

For x=1 and x=4/3, combined neutron and X-ray diffraction refinements were carried out to determine the crystal structure. This allowed for B and O positions to be determined from the neutron data and Mg and Mn positions and occupancies from PXRD. For x=2/3, where only PXRD data was available, B and O positions from the x=1 combined neutron refinement were used, with other parameters refined against the PXRD data.

The refined volumes shown in the inset of Figure 1 vary according to Vegard's law, with higher Mn content increasing the unit cell volume. The volume of *M*1 and *M*2 polyhedra and average *M*-O bond distances also change systematically with increasing Mn content, Table 1. In all cases, the Mg and Mn ions are disordered over the M1 and *M*2 sites, Figure 1, Table 1. This is in agreement with previous analysis by Utzolino and Bluhm.[18] However, a slight preference for Mn to occupy the more distorted, but larger, *M*1 site is observed for all the mixed-metal samples. This is exemplified by $MgMnB_2O_5$, where total disorder would give occupancies of 0.5 in each site whereas a 0.65/0.35 split is observed. Having mixed cations on the sites could hinder ion diffusion by blocking channels so the presence of some order could be beneficial. However, higher Mg content on *M*2 may also aid Mg removal and Li insertion as bond valence sum calculations carried out by Bo *et al.*[23] suggest that the Mg ion diffusion pathway occurs via interstitial sites linked with the *M*2 site. Full structural details are given in Tables S1, S2 and S3.

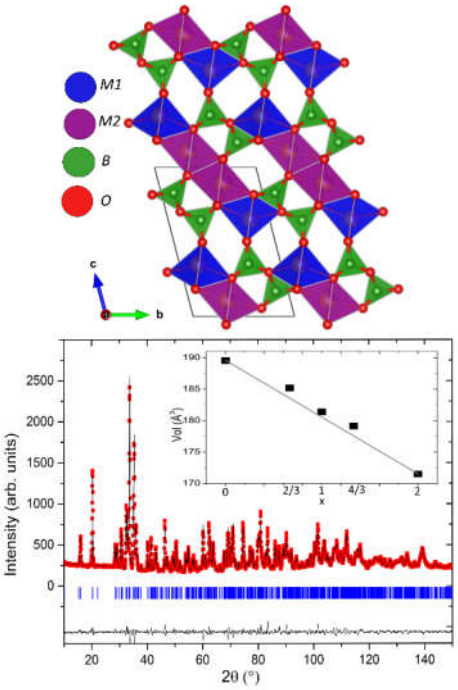

Figure 1. a) Polyhedral model of the $M_2B_2O_5$ structure. $M1O_6$, $M2O_6$ and BO_3 polyhedra are shown in purple, blue and green respectively. b) Neutron diffraction pattern (red dots) and fit (black line) of $Mg_{4/3}Mn_{2/3}B_2O_5$. Allowed Bragg reflections are shown as blue tick marks. Inset shows the change in cell volume in $Mg_xMn_{2-x}B_2O_5$ as a function of *x* determined from neutron and powder diffraction.

Table 1. Summary of refined crystal structure parameters determined from PXRD and powder neutron diffraction at room temperature for the solid solution $Mg_xMn_{2-x}B_2O_5$, formed between $Mg_2B_2O_5$ and $Mn_2B_2O_5$.

$Mg_xMn_{2-x}B_2O_5$	$x = 0$[21]	$x = \frac{2}{3}$	$x = 1$	$x = \frac{4}{3}$	$x = 2$[21,28]
Space group	$P\bar{1}$	$P\bar{1}$	$P\bar{1}$	$P\bar{1}$	$P\bar{1}$
χ^2		2.15	3.33	11.7	
R_{wp}		20.1	19.7	9.88	
Vol (Å^3)	189.53	185.172(9)	181.365(10)	179.131(6)	171.48/171.33
M1 occ (Mn/Mg)	1/0	0.73/0.28(10)	0.647/0.353(8)	0.403/0.597(6)	0/1
M2 occ (Mn/Mg)	1/0	0.61/0.39(10)	0.353/0.647(8)	0.264/0.736(6)	0/1
Average M1-O (Å)	N/A	2.196(10)	2.173(5)	2.131(7)	2.1292(15)
Average M2-O (Å)	N/A	2.160(10)	2.142(5)	2.139(7)	2.0946(15)

$MgMnB_2O_5$ Electrochemistry

$MgMnB_2O_5$ was first investigated as a potential cathode due to it having the highest theoretical capacity of the series. On first charge vs Li^+ a capacity of 330 mAhg^{-1} was achieved at a rate of C/25, suggesting complete removal of Mg from the structure (theoretical capacity of 296.6 mAhg^{-1}), Figure 2. The labile nature of Mg differs from previous Mg containing Li-ion cathodes, such as Mg doped $LiCoO_2$ or $LiFePO_4$[29,30], where Mg is thought to be electrochemically inactive, providing structural stability only. The slight excess of capacity on 1st charge varies with each cell and is therefore attributed to side reactions with the electrolyte rather than a deviation from a 1:1 Mg:Mn stoichiometry.

The subsequent discharge process consists of Li^+ ion insertion into the de-magnesiated Mn^{IV} framework. On 1st discharge 220 mAhg^{-1} of Li^+ were inserted equating to 1.2 Li ions per unit cell, which is smaller than the theoretical capacity calculated by assuming insertion of 2 Li^+ ions for each Mg^{2+} ion (342.5 mAhg^{-1}). The sloping nature of the electrochemistry profile can be attributed to Mg/Mn site disorder and the different local environments of Li.[31]

The Li ions are then fully removed on 2nd charge (221 mAhg^{-1}). Over subsequent cycles the capacity gradually increased reaching a maximum of 1.47 Li ions, 252 mAhg^{-1} after 12 cycles. The increase in capacity is accompanied by a change in voltage profile. The initially lower capacity is attributed to de-intercalated Mg^{2+} ions being present in high enough concentration near the cathode to continue to be involved in cycling, and their sluggish reinsertion into the framework resulting in larger overpotential. As the cycle number increases the Mg ions diffuse into the bulk electrolyte leaving a significant excess of Li ions as the main electro-active species. This hypothesis is supported by figure S1 which shows that no change in voltage profile occurs over the first 10 cycles when a new coin cell is assembled with washed de-magnesiated cathode and fresh Li electrolyte, as the residual Mg ions were removed. The reduced capacity is attributed to film degradation during coin cell disassembly and washing.

After 100 cycles the capacity and slope of the charge and discharge processes stabilised at a reversible capacity of 194 mAhg^{-1}. Discharge to 1.5 V results in $Li_{1.1}Mn^{(+2.9)}B_2O_5$. Two subtle changes in slope are observed in the dQ/dV vs V plots at ~2.8 V and 4.2 V on charge, and at 2.5 V and 4.0 V on discharge (Figures S2 and S3), which may correspond to the $Mn^{2+} \leftrightarrow Mn^{3+}$ and $Mn^{3+} \leftrightarrow Mn^{4+}$ processes. This suggests relatively low overpotential for the high voltage process, consistent with galvanostatic intermittent titration (GITT) experiments, Figure 4. The 300 mV overpotential on Li removal and 200 mV overpotential for Li insertion are comparable to overpotentials in the early stages of *m*-$LiMnBO_3$ cycling.[32] However, the large increases in overpotential at deep charge and discharge seen in other borates, which limit capacity, are not observed here.

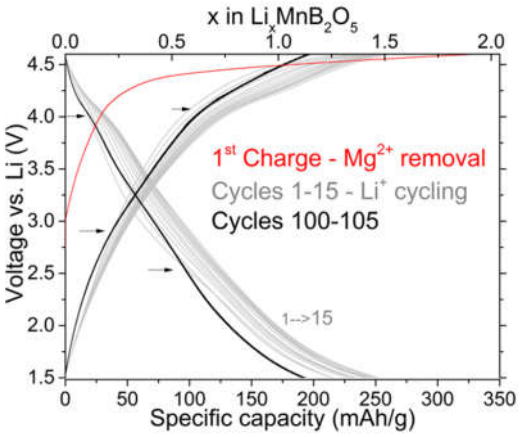

Figure 2. Cycling of $MgMnB_2O_5$ at C/25. Initial charge (Mg removal) - Red line. Subsequent cycling vs Li for 10 cycles - Grey lines). Cycling vs Li after 100 cycles - Black line. Arrows indicate changes in slope, with values extracted from dQ/dV plot, Figure 3.

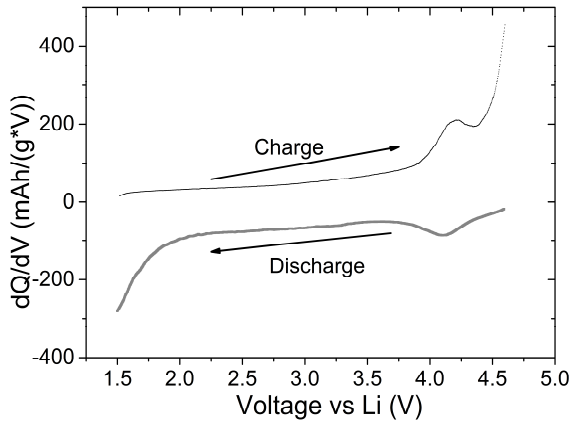

Figure 3. dQ/dV plot of the 10th cycle of a $MgMnB_2O_5$ vs Li cell, cycled at C/25.

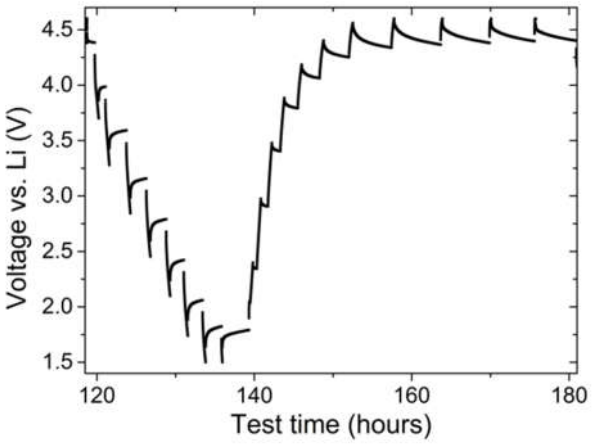

Figure 4. 3rd cycle of a GITT experiment of $MgMnB_2O_5$ vs Li showing the equilibrium voltage for Li insertion and removal. Cycled at C/25 with up to 100-hour rest periods.

At the higher rate of C/5, the Mg removal capacity is reduced to 177 $mAhg^{-1}$, 0.6 Mg^{2+} ions per formula unit, as shown in Figure 5. This is followed by lithium insertion of 125 $mAhg^{-1}$, 56.8% of the capacity achieved at C/25. Continued cycling at C/5 for 1000 cycles shows a gradual increase in capacity up to 314 $mAhg^{-1}$. This equates to reversible insertion of 1.82 Li^+ with a specific energy of 802 $WhKg^{-1}$, assuming all the Mg^{2+} is removed during the 1000 cycles. Increased capacity with extended cycling is often ascribed to electrochemical grinding, however the small volume change (Figure 7) means this is unlikely to be the cause in this case. An alternative mechanism could be a change in cation environment caused by mobility in the disordered metal sites or structural rearrangement that offers more Li sites. Detailed structural analysis of the cycled material to determine the sites for Li was hindered by small particle size and amorphisation, as seen in the ex-situ diffraction patterns (Figure S2). The ^7Li MAS NMR spectra of the material acquired after one charge-discharge cycle do not contain sufficient resolution to determine where the Li ions are located.

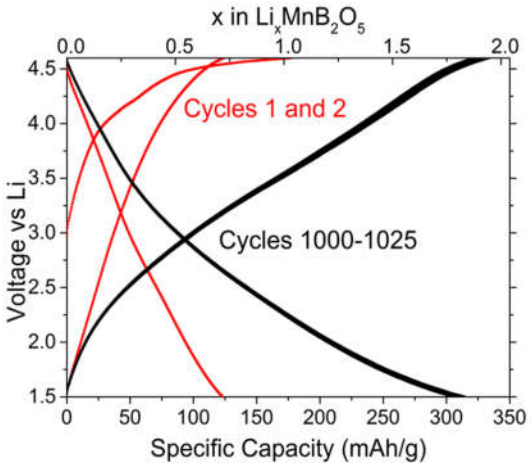

Figure 5. Cycling of $MgMnB_2O_5$ vs Li at C/5 between 1.5 and 4.6 V. Initial charge and subsequent discharge and 2nd charge - red line. Cycles 1000-1025 - black lines.

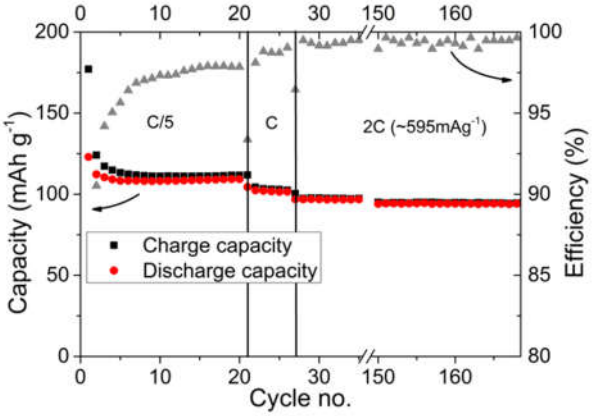

Figure 6. Rate study at C/5, C and 2C for $MgMnB_2O_5$ over the first 180 cycles. Left axis, charge and discharge capacity. Right axis, efficiency on expanded scale.

The rate capability of $MgMnB_2O_5$ over the first 180 cycles is shown in Figure 6. The initial cycles at C/5 likely still involve Mg^{2+}. After 6 cycles the capacity settles at ~111 $mAhg^{-1}$ and increasing the charge rate to 2C leads to a 12 % reduction in capacity, 97.4 $mAhg^{-1}$.

Electrochemical tests were also carried out to investigate Li intercalation into as prepared $MgMnB_2O_5$. 0.3 Li^+ (47.1 mAg^{-1}) can be inserted into the $MgMnB_2O_5$ electrode at C/25 (inset Figure 7) before de-magnesiation (*i.e.* discharging the cell first), which suggests the presence of Mn^{3+} in the pristine material caused by small deviations from ideal stoichiometry. The capacity may also arise from Li intercalation into carbon. However, it is believed to involve at least some intercalation into $MgMnB_2O_5$ as ex-situ diffraction, discussed in the following section, shows a change in unit cell volume and an additional peak associated with doubling the unit cell.

Ex-situ Diffraction

Ex-situ powder X-ray and neutron diffraction were carried out to assess structural changes on de-magnesiation and lithium insertion. Figure S2 shows neutron diffraction data fitted with a profileless pattern matching[27] refinement

of the de-magnesiated material $Mg_xMnB_2O_5$ (charged), $Li_xMnB_2O_5$ (lithium inserted after de-magnesation, charge-discharged) and $Li_xMgMnB_2O_5$ (lithium insertion into $MgMnB_2O_5$, discharge only). All 3 patterns have a peak at ~18.5° which is not observed in the pristine material. This is characteristic of a doubling of the unit cell in the *c* direction. Further characterisation of the change in structure is not possible due to the quality of the pattern and the small size of the active material particles in the electrode.

The change in volume per unit cell associated with each cycling stage is given in Figure 7. On removal of Mg to form MnB_2O_5 there is a 4.2% reduction in volume. Subsequent Li insertion increases the volume by just 1%. This is a small volume change for a relatively high capacity electrode material. It is also worth noting that the polyanion framework is retained even after removing 50% of the cations.

Inserting Li into the pristine $MgMnB_2O_5$ results in a 5% volume decrease, supporting the observation that some Li is inserted into the active material rather than carbon or reacting with electrolyte to form an SEI layer. This suggest the presence of a small amount of Mn^{3+} in the starting material. The reduction in volume can be rationalized by the additional positive charge shielding the electrostatic repulsion between the oxygen anions, and attracting the polyanion blocks closer together. This has previously been observed for CoO_2 where Li insertion reduces the metal oxide layer serpation.[33]

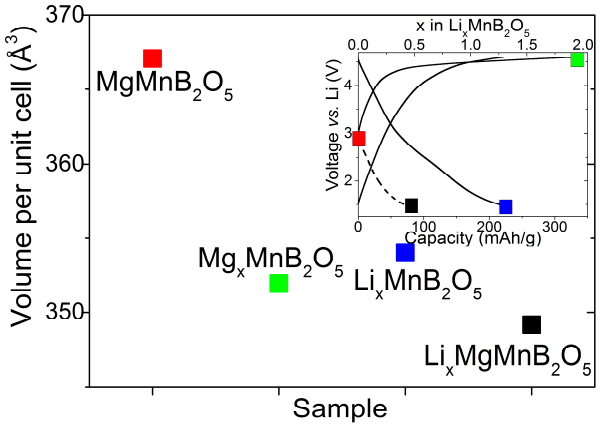

Figure 7. Volume change for $MgMnB_2O_5$ on cycling at C/25 between 1.5 V and 4.6 V, determined by profileless pattern fitting of neutron diffraction data. Inset shows the point of cycle each sample was taken from.

<u>^{7}Li NMR</u>

The assertion that Li is inserted into the framework on cycling is further supported by ^{7}Li MAS NMR spectra (Figure S3). The intensity of Li resonance from the charged-discharged material is significantly greater than that from the charged sample, meaning a large amount of Li has been inserted into the structure. The charged sample contains just 3% of the Li inserted during discharge. The resonance of the discharged sample appears to have two components both with short spin-lattice (T_1) and spin-spin (T_2) relaxation times (T_1 = 1.63 s and 20ms, and T_2 = 519 ms and 804 µs), characteristic of Li interacting with a paramagnetic centre. The majority of this intercalation is reversible, demonstrated by the decrease in Li signal on 2nd charge to almost that of the 1st charge.

The spectra obtained for the discharged first sample (i.e. before Mg removal) shows a low intensity peak with similar resonance to that seen in the cycled samples, which is ascribed to a small amount of Li insertion, further supporting the presence of Mn^{3+} in the pristine material, as indicated by electrochemistry and diffraction.

Comparing the 1st discharge with the 100th discharge (figure S4) shows that in later cycles Li insertion quantities are ~80% of those achieved on 1st discharge. This agrees with the electrochemistry measurement where capacities were greater for initial discharges than those after 100 cycles. The value obtained from the capacity change between 1st discharge and 100th is ~88%, the difference in these values can be attributed to cell to cell variation.

<u>SQUID Magnetometry</u>

If the Mg is removed from the structure, the remaining Mn should undergo oxidation to balance the loss of the 2+ ion. On Li insertion there should be a corresponding Mn reduction. Therefore, measurement of the Mn magnetic moment will give some indication of the redox reaction occurring during cycling.[34] The expected magnetic moments for high spin Mn^{2+}, Mn^{3+}, and Mn^{4+} are 5.9 µB, 4.9 µB and 3.9 µB respectively, assuming no spin orbit coupling ($\mu_{so} = g\sqrt{s(s+1)}$).

Figure S5 shows the inverse magnetic susceptibility, χ^{-1}, for uncycled x=1 cathode material, 1st charge, subsequently discharged and 2nd charge ex-situ samples. The calculated moment for the uncycled material is 6.0 µB, equating to Mn^{2+}, as expected. On charge (Mg removal) Mn oxidation occurs to between Mn^{3+} and Mn^{4+} (a calculated magnetic moment of 4.5 µB). On 1st discharge (Li insertion) the oxidised Mn is reduced to between Mn^{2+} and Mn^{3+} (5.5 µB). The fact that Mn is not fully reduced back to Mn^{2+} fits with the electrochemical data, where 1st charge has a greater capacity than 1st discharge. On 2nd charge the Mn is oxidised back to between Mn^{3+} and Mn^{4+}, further demonstrating reversible intercalation.

The calculated moment for the discharged only sample is 6.2 µB, greater than the 6.0 µB of the pristine material. This suggests that some reduction of Mn may be occurring and that calculated values for all samples are slightly overestimated. This may be due residual magnetic interactions meaning fits were not in a regime where the Curie-Weiss analysis is valid. This has previously been observed in other Mn systems with large Weiss temperatures.[35] Therefore, although the calculated value for the uncycled material is 6.0 µB, it is possible that it contains a small amount of Mn^{3+}.

<u>$Mg_{4/3}Mn_{2/3}B_2O_5$ Electrochemistry</u>

Cycling $Mg_{4/3}Mn_{2/3}B_2O_5$ at C/25 (Figure 8) gives a Mg removal capacity of 161.4 $mAhg^{-1}$ (0.51Mg), which is 78% of the theoretical capacity (187 $mAhg^{-1}$). Subsequently 130 $mAhg^{-1}$ of Li are inserted into the structure, which equates to 0.74 Li assuming $Mg_{2/3}Mn_{2/3}B_2O_5$ or 0.76 Li assuming $Mg_{0.8}Mn_{2/3}B_2O_5$ as calculated from 1st charge capacity. This is fully reversible with the same sloping charge and discharge slopes seen in $MgMnB_2O_5$. As for $MgMnB_2O_5$, the

capacity increases reaching a discharge capacity of 145 mAh g^{-1} after 10 cycles.

By running at the slower rate of C/100 a slightly higher Mg removal capacity of 169.3 $mAhg^{-1}$ (0.54 Mg) is obtained, 81% of theoretical capacity. As with $MgMnB_2O_5$, the majority of the Mg removal capacity is above 4V, with just 30 $mAhg^{-1}$ (~20%) below 4V. Li insertion capacities are also increased significantly on cycling, with 166.1 $mAhg^{-1}$ (0.95 Li assuming $Mg_{2/3}$ or 0.97 Li assuming $Mg_{0.8}$) on first discharge, further increasing to 194.8 $mAhg^{-1}$ (1.11 Li assuming $Mg_{2/3}$ or 1.15 Li assuming $Mg_{0.8}$) at the end of the 10th discharge. Li insertion on the 10th discharge occurs with a shoulder at 4.1V and a change in slope at 3 V, higher voltages than those observed for $MgMnB_2O_5$ (4.0 and 2.5 V). On charge there is continuous capacity from 1.5 V with no obvious changes in slope until around 4 V, with a shoulder in dQ/dV at 4.25 V, Figure 9. The higher voltage discharge and lower voltage charge is explained by the lower overpotential (150 mV) observed in the GITT curve, figure S6.

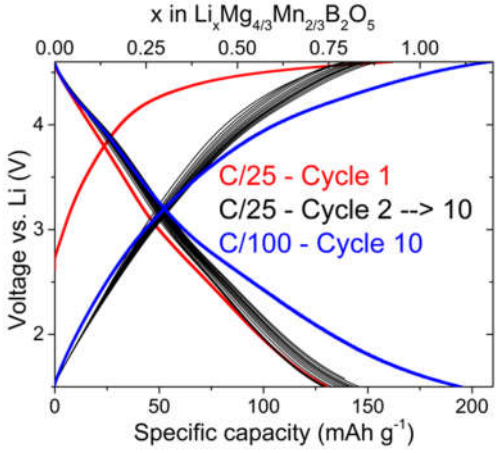

Figure 8. Cycling of $Mg_{4/2}Mn_{2/3}B_2O_5$ at a rate of C/25 and C/100 vs Li. 1st cycle of Mg removal at and initial Li insertion at C/25 in red, subsequent C/25 cycles in black, 10th cycle at C/100 in blue.

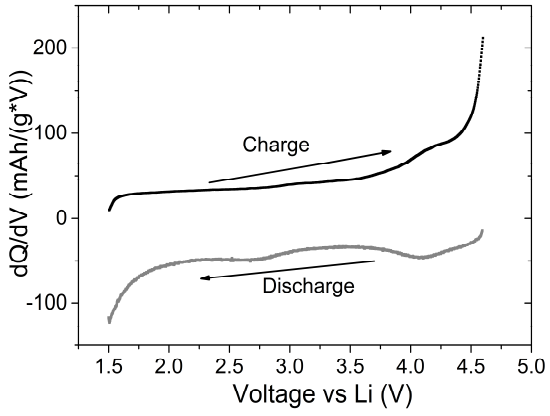

Figure 9. dQ/dv plot of the 10th cycle of $Mg_{4/3}Mn_{2/3}B_2O_5$ vs Li at C/25.

$Mg_{2/3}Mn_{4/3}B_2O_5$ Electrochemistry

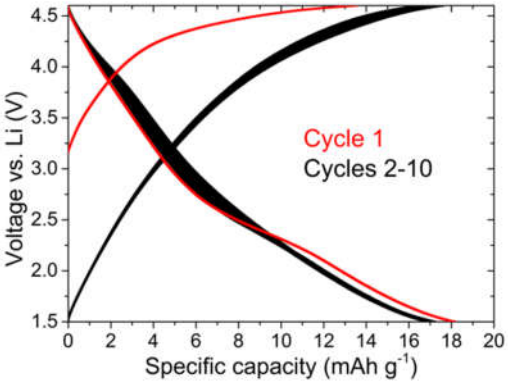

Figure 10. Cycling behaviour of $Mg_{2/3}Mn_{4/3}B_2O_5$ at a C/50 rate. Cycle 1 Mg removal and subsequent Li instertion – red curve, Cycles 2-10 vs Li – black curve.

The Mn rich pyroborate $Mg_{2/3}Mn_{4/3}B_2O_5$ has a Mg removal theoretical capacity of 187.3 $mAhg^{-1}$ and insertion of 1.33 Li into $Mn_{4/3}B_2O_5$ would give 204.05 $mAhg^{-1}$.

Figure 10 shows that $Mg_{2/3}Mn_{4/3}B_2O_5$ has significantly lower reversible capacity than $MgMnB_2O_5$, achieving just 17.6 $mAhg^{-1}$ after 10 cycles, even at a slower rate of C/50. Though there is little capacity, the discharge curves still show two processes similar to those seen in the Mg rich compounds. This suggests there are real and reversible electrochemical reactions occurring, but that they are significantly hindered. GITT experiments show a very large overpotential (>1V) associated with both Mg removal and Li insertion, Figure 11. This is significantly higher than the Mg rich compounds and indicates poor ionic and/or electronic conductivity. Mg and Li diffusion could be limited to the surface of the particles due to the excess of Mn blocking the Li/Mg diffusion pathways in the structure.[23] In addition, the change in structure that leads to a doubling of the unit cell on cycling may vary the interstitial site potentials, resulting in diffusion being unfavourable.

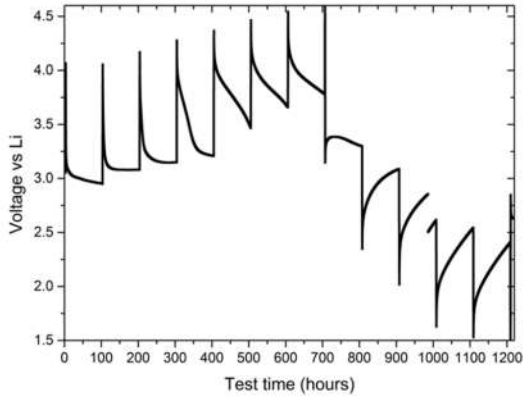

Figure 11. Galvanostatic Intermittent Titration experiment on $Mg_{2/3}Mn_{4/3}B_2O_5$ on 1st charge and discharge vs Li. Over 1.0 V of overpotential is observed on both 1st charge and discharge.

CONCLUSIONS

Three points of the solid solution $Mg_xMn_{2-x}B_2O_5$ have been synthesised and shown to crystallise in the $P\bar{1}$ space

group. Mg and Mn are disordered over the two metal sites, however there is a slight preference for Mn to occupy the more distorted, but larger, site M1.

Electrochemical measurements vs a Li metal anode show that the low Mg content (x=2/3) material has very little capacity for either Mg removal or Li insertion. The higher Mg content (x=4/3 and 1) versions, both display significant Li cycling capacity between 1.5 V and 4.6 V. $MgMnB_2O_5$ has a maximum Li discharge capacity of ~240 $mAhg^{-1}$ which settles to a consistent 193 $mAhg^{-1}$, or 1.1 Li after 100 cycles. At high rate of C/5, capacities of >100 $mAhg^{-1}$ are maintained over 1000 cycles and gradually increases to >300 $mAhg^{-1}$. The cause of this increase is unknown though is suspected to be due to a change in particle size, crystallinity or Mn site migration. The x=4/3 material also shows good Li reversibility with ~0.75 Li inserted at C/25, increasing to nearly 1 Li per unit at slower rate of C/100, giving a capacity of 188.6 $mAhg^{-1}$.

Structural analysis from powder neutron and X-ray diffraction were used to show that the pyroborate undergoes a volume change on both Mg removal and Li insertion. ^{7}Li NMR of x=1 charged and discharged samples show that reversible insertion of Li into the structure. This, along with the oxidation and reduction of Mn calculated from the SQUID Magnetometry demonstrate that Mg is removed from the structure on charge, and replaced by Li on discharge.

The use of polyanion structures where Li can replace labile Mg, without disrupting crystal structure, opens up a new avenue for novel Li-ion cathode material with high energy densities. Facile Mg removal in $Mg_xMn_{x-1}B_2O_5$ means that these materials may also be of interest for Mg-ion battery systems[36].

This study shows the pyroborates are a promising family of materials for high capacity, high rate, Li-ion cathodes. The light weight borate framework leads to significantly higher gravimetric capacities than that observed for the pyrophspate polyanions. Further improvements could be made by understanding the origin of the capacity increases over 1000's of cycles, by altering the transition metal to tune the voltage and capacity, as has been successfully demonstrated in $LiMBO_3$[37] or by improving the ionic and/or electronic conductivity via optimised composite and film construction.

ASSOCIATED CONTENT

SUPPORTING INFORMATION

The Supporting Information is available free of charge on the ACS Publications website at DOI: #########

Full data from structural refinements, cycling of x=1 with fresh electrolyte after fist charge, dQ/dV plots, ex-situ powder neutron diffraction, ^{7}Li NMR spectra, and $1/\chi$ vs T magnetization plot for x=1 samples, dQ/dV and GITT for x=4/3.

AUTHOR INFORMATION

*E-mail: sed33@cam.ac.uk

Notes

The authors declare no competing financial interest.

Acknowledgements

This work was supported by the EPSRC Cambridge NanoDTC, EP/G037221/1 and The Winton Programme for the Physics of Sustainability. The authors wish to thank Paromita Mukherjee for assisting with the collection of neutron data. The data used in this publication is available at DOI:10.17863/CAM.8261
Data collected at the Institut Laue-Langevin (ILL) can be accessed at DOI:10.5291/ILL-DATA.5-21-1099. Magnetic measurements were carried out using the Advanced Materials Characterisation Suite, funded by EPSRC Strategic Equipment Grant EP1M000524111.

REFERENCES

(1) Armand, M.; Tarascon, J.-M. Building Better Batteries. *Nature* **2008**, *451*, 652–657.

(2) Thackeray, M. M.; Thomas, J. O.; Whittingham, M. S. Science and Applications of Mixed Conductors. *MRS Bull.* **2000**, *25*, 39–46.

(3) Thackeray, M. M.; David, W. I. F.; Bruce, P. G.; Goodenough, J. B. Lithium Insertion into Manganese Spinels. *Mater. Res. Bull.* **1983**, *18*, 461–472.

(4) Delmas, C. Electrochemical and Physical Properties of the LixNi1-yCoyO2 Phases. *Solid State Ionics* **1992**, *53–56*, 370–375.

(5) Shaju, B. K. M.; Bruce, P. G. Macroporous Li(Ni1/3Co1/3Mn1/3)O2:A High-Power and High-Energy Cathode for Rechargeable Lithium Batteries. *Adv. Mater.* **2006**, *18*, 2330–2334.

(6) Yabuuchi, N.; Ohzuku, T. Novel Lithium Insertion Material of LiCo1/3Ni1/3Mn1/3O2 for Advanced Lithium-Ion Batteries. *J. Power Sources* **2003**, *119–121*, 171–174.

(7) Martha, S. K.; Haik, O.; Zinigrad, E.; Exnar, I.; Drezen, T.; Miners, J. H.; Aurbach, D. On the Thermal Stability of Olivine Cathode Materials for Lithium-Ion Batteries. *J. Electrochem. Soc.* **2011**, *158*, A1115–A1122.

(8) Lee, M.; Lee, S.; Oh, P.; Kim, Y.; Cho, J. High Performance LiMn 2 O 4 Cathode Materials Grown with Epitaxial Layered Nanostructure for Li-Ion Batteries. *Nano Lett.* **2013**, *14*, 993–999.

(9) Chen, C. H.; Liu, J.; Stoll, M. E.; Henriksen, G.; Vissers, D. R.; Amine, K. Aluminum-Doped Lithium Nickel Cobalt Oxide Electrodes for High-Power Lithium-Ion Batteries. *J. Power Sources* **2004**, *128*, 278–285.

(10) Padhi, A. K.; Nanjundaswamy, K. S.; Goodenough, J. B. Phospho-Olivines as Positive-Electrode Materials for Rechargeable Lithium Batteries. *J. Electrochem. Soc.* **1997**, *144*, 1188–1194.

(11) Yamada, A.; Chung, S. C.; Hinokuma, K. Optimized LiFePO4 for Lithium Battery Cathodes. *J. Electrochem. Soc.* **2001**, *148*, A224–A229.

(12) Huang, H.; Yin, S.-C.; Nazar, L. F. Approaching Theoretical Capacity of LiFePO4 at Room Temperature at High Rates. *Electrochem. Solid-State Lett.* **2001**, *4*, A170–A172.

(13) Legagneur, V.; An, Y.; Mosbah, A. LiMBO3(M= Mn, Fe, Co): Synthesis, Crystal Structure and Lithium Deinsertion/insertion Properties. *Solid State Ionics* **2001**, *139*, 37–46.

(14) Afyon, S.; Kundu, D.; Krumeich, F.; Nesper, R. Nano LiMnBO3, a High-Capacity Cathode Material for Li-Ion Batteries. *J. Power Sources* **2013**, *224*, 145–151.

(15) Dong, Y. Z.; Zhao, Y. M.; Shi, Z. D.; An, X. N.; Fu, P.; Chen, L. The Structure and Electrochemical Performance of LiFeBO3 as a Novel Li-Battery Cathode Material. *Electrochim. Acta* **2008**, *53*, 2339–2345.

(16) Bo, S.-H.; Wang, F.; Janssen, Y.; Zeng, D.; Nam, K.-W.; Xu, W.; Du, L.-S.; Graetz, J.; Yang, X.-Q.; Zhu, Y.; Parise, J. B.; Grey, C. P.; Khalifah, P. G. Degradation and (De)lithiation

Processes in the High Capacity Battery Material $LiFeBO_3$. *J. Mater. Chem.* **2012**, *22*, 8799–8809.
(17) Barpanda, P.; Yamashita, Y.; Yamada, Y.; Yamada, A. High-Throughput Solution Combustion Synthesis of High-Capacity $LiFeBO_3$ Cathode. *J. Electrochem. Soc.* **2013**, *160*, A3095–A3099.
(18) Utzolino, A.; Karsten, B. Synthesis and Crystal Structure of Manganese Pyrobates $MnCo(B_2O_5)$ and $MnMg(B_2O_5)$. *Z.Naturforsch* **1996**, No. 51 b, 912–916.
(19) Fernandes, J.; Sarrat, F.; Guimarães, R.; Freitas, R.; Continentino, M.; Doriguetto, a.; Mascarenhas, Y.; Ellena, J.; Castellano, E.; Tholence, J.-L.; Dumas, J.; Ghivelder, L. Structure and Magnetism of $MnMgB_2O_5$ and $Mn_2B_2O_5$. *Phys. Rev. B* **2003**, *67*, 104413.
(20) Kawano, T.; Morito, H.; Yamada, T.; Onuma, T.; Chichibu, S. F.; Yamane, H. Synthesis, Crystal Structure and Characterization of Iron Pyroborate ($Fe_2B_2O_5$) Single Crystals. *J. Solid State Chem.* **2009**, *182*, 2004–2009.
(21) Block, S.; Burley, G.; Perloff, A.; Mason, R. D. Refinement of the Crystal Structure of Triclinic Magnesium Pyroborate. *J. Res. Natl. Bur. Stand. (1934).* **1959**, *62*, 95–100.
(22) Yamada, A.; Nishimura, S. New Lithium Iron Pyrophosphate $Li_2FeP_2O_7$ as 3.5 V Class Cathode Material for Lithium-Ion Battery. *JACS Commun.* **2010**, *132*, 13596–13597.
(23) Bo, S.-H.; Grey, C. P.; Khalifah, P. G. Defect-Tolerant Diffusion Channels for Mg_{2+} Ions in Ribbon-Type Borates: Structural Insights into Potential Battery Cathodes $MgVBO_4$ and $MgxFe_{2-x}B_2O_5$. *Chem. Mater.* **2015**, *27*, 4630–4639.
(24) Rietveld, H. A Profile Refinement Method for Nuclear and Magnetic Structures. *J. Appl. Crystallogr.* **1969**, *2*, 65–71.
(25) Rodríguez-Carvajal, J. Recent Advances in Magnetic Structure Determination by Neutron Powder Diffraction. *Phys. B Condens. Matter* **1993**, *192*, 55–69.
(26) Scherrer, P. *Determination of the Size and the Internal Structure of Colloid Particles by X-Ray Radiation*; Springer Berlin Heidelberg, 1912.
(27) Le Bail, A.; Duroy, H.; Fourquet, J. L. Ab-Initio Structure Determination of LiSbWO6 by X-Ray Powder Diffraction. *Mater. Res. Bull.* **1988**, *23*, 447–452.
(28) Guo, G. C.; Cheng, W. D.; Chen, J. T.; Huang, J. S.; Zhang, Q. E. Triclinic $Mg_2B_2O_5$. *Acta Crystallogr. Sect. C Cryst. Struct. Commun.* **1995**, *51*, 351–353.
(29) Luo, W.; Li, X.; Dahn, J. R. Synthesis and Characterization of Mg Substituted $LiCoO_2$. *J. Electrochem. Soc.* **2010**, *157*, A782–A790.
(30) Arumangam, D.; Paruthimal, K.; Manisankar, P. Synthesis and Electrochemical Characterizations of Nano-Crystalline $LiFePO_4$ and Mg-Doped $LiFePO_4$ Cathode Materials for Rechargeable Lithium-Ion Batteries. *J Solid State Electrochem* **2009**, *13*, 301–307.
(31) Liu, C.; Neale, Z. G.; Cao, G. Understanding Electrochemical Potentials of Cathode Materials in Rechargeable Batteries. *Mater. Today* **2016**, *19*, 109–123.
(32) Kim, J. C.; Seo, D. H.; Chen, H.; Ceder, G. The Effect of Antisite Disorder and Particle Size on Li Intercalation Kinetics in Monoclinic $LiMnBO_3$. *Adv. Energy Mater.* **2015**, 5, 1401916–1401924.
(33) Reimers, J. N.; Dahn, J. Electrochemical and In Situ X-Ray Diffraction Studies of Lithium Intercalation in Li_xCoO_2. *J. Electrochem. Soc.* **1992**, *139*, 2091–2097.
(34) Chernova, N. A.; Nolis, G. M.; Omenya, F. O.; Zhou, H.; Li, Z.; Whittingham, M. S. What Can We Learn about Battery Materials from Their Magnetic Properties? *J. Mater. Chem.* **2011**, *21*, 9865–9875.
(35) Lee, J.; Seymour, I.; Pell, A.; Dutton, S.; Grey, C. A Systematic Study of 25Mg NMR in Paramagnetic Transition Metal Oxides: Applications to Mg-Ion Battery Materials. *Phys. Chem. Chem. Phys.* **2017**, *19*, 613–625.
(36) Yoo, H. D.; Shterenberg, I.; Gofer, Y.; Gershinsky, G.; Pour, N.; Aurbach, D. Mg Rechargeable Batteries: An on-Going Challenge. *Energy Environ. Sci.* **2013**, *6*, 2265–2279.
(37) Le Roux, B.; Bourbon, C.; Lebedev, O. I.; Colin, J. F.; Pralong, V. Synthesis and Characterization of the $LiMnBO_3$-$LiCoBO_3$ Solid Solution and Its Use as a Lithium-Ion Cathode Material. *Inorg Chem* **2015**, *54*, 5273–5279.

Insert Table of Contents artwork here